Calculated Chemical and Vibrational Nonequilibrium Effects in Hypersonic Nozzles

Oussama Rizkalla,* Wallace Chinitz,† and John I. Erdos‡
General Applied Science Laboratories, Inc., Ronkonkoma, New York 11779

A method of characteristics computer program has been developed for designing shock-free scramjet engine nozzles, including the effects of finite-rate chemistry and vibrational relaxation. The program incorporates a compressible, turbulent boundary-layer calculation to determine boundary-layer displacement thickness, and skin friction coefficient. Results obtained for a generic nozzle designed for a Mach 20 flight condition lead to the conclusions that finite-rate chemical recombination and viscous effects are of major consequence in determining nozzle design and performance, but that the vibrational mode is in equilibrium throughout the nozzle. In addition, nozzle design may be tailored to produce a certain geometry and performance characteristics by specifying a priori parameters such as design exit pressure ratio and maximum permissible wall angle.

Nomenclature

C_F = thrust coefficient
C_M = moment coefficient around nozzle throat
c_p = constant pressure specific heat [normalized by c_{p_∞} in Eqs. (9-11), (17), and (19)]
F = force, N
H = stagnation enthalpy normalized by $R_o T_\infty$
h = static enthalpy normalized by $R_o T_\infty$
h_f = standard heat of formation normalized by $R_o T_\infty$
J = an index, $=0$ for two-dimensional flow
$=1$ for axisymmetric flow
M = Mach number
$\dot{m}_f$ = fuel mass flow rate, kg/s
P = pressure (normalized by $\rho_\infty u_\infty^2$)
Q = dynamic pressure, N/m^2
q = velocity normalized by u_∞
R = mixture gas constant, J/kg/K
R_i = gas constant of species i, J/kg/K
R_o = Universal gas constant, J/kgmole/K
R_{TH} = throat height from centerline (two dimensional) or throat radius (axisymmetric), m
r,y = radial or normal coordinate normalized by R_{TH}
rad = radius of the initial circular arc normalized by R_{TH}
T = temperature normalized by T_∞, except K in equations relating to vibrational nonequilibrium corrections
t = time, s
u = axial velocity component normalized by u_∞
u_v = internal energy, J/kg
v = normal velocity component normalized by u_∞
W = mixture molar mass (molecular weight)
W_i = molar mass of species i, kg/kgmole
x = axial coordinate normalized by R_{TH}
α_i = mass fraction of species i
γ = specific heat ratio
θ = flow inclination relative to the axial direction
Θ_i = characteristic vibrational temperature of species i
μ = Mach angle
ρ = density normalized by ρ_∞
ϕ = fuel-air equivalence ratio
$\dot{\omega}_i$ = chemical source term for species i, kg/s

Subscripts

c = cowl
e = nozzle exit conditions
i = species index
o = throat conditions
v = vibrational
w = nozzle wall
∞ = freestream conditions

Superscript

$*$ = dimensional quantity

I. Introduction

THE design of scramjet engine nozzles for hypersonic flight vehicles must require analyses that incorporate nonequilibrium chemistry and vibrational relaxation. Frequently, the gas composition in the nozzle is assumed to be frozen at the combustor exit conditions or to freeze chemically a short distance downstream of the nozzle throat.[1] This frozen-chemistry assumption is based upon prior experience with nozzles for rocket engines and subsonic combustion ramjets, as well as hypersonic wind tunnels. However, the high nozzle inlet Mach number in a scramjet engine operating at high flight Mach numbers (i.e., $M \geq 10$) produces shallow wave angles that result in long nozzles that must be integrated with the airframe. This gradual expansion, unlike a rocket engine nozzle, reduces the tendency toward chemically frozen flow and may result in significant recovery of energy from dissociated states and vibrational excitation present in the combustor. Hence, in these situations, it is important that scramjet nozzle design incorporates or considers finite-rate chemistry and vibrational nonequilibrium effects. In addition, long nozzles may result in large viscous effects that must be considered.

A method-of-characteristics (MOC) solution employed to solve the equations governing nozzle expansions in the presence of finite-rate chemistry and vibrational relaxation is described herein. As detailed in Sec. II, the MOC procedure employs suitably modified compatibility and energy conservation equations to account for the chemical changes, adjustments to enthalpies, specific heats, and entropies of vibrating polyatomic species, and an appended compressible, turbulent boundary-layer calculation to estimate displacement thickness and assess the effects of wall shear stresses on force and mo-

---

Presented as Paper 88-3263 at the AIAA/ASEE/ASME/SAE 24th Joint Propulsion Conference, Boston, MA, July 11-14, 1988; received Aug. 28, 1988; revision received Jan. 26, 1989.

*Research Scientist. Member AIAA.

†Principal Research Scientist; Professor of Mechanical Engineering, Cooper Union, School of Engineering. Associate Fellow AIAA.

‡Vice President. Associate Fellow AIAA.

ment coefficients. In Sec. III, calculations are presented that were carried out to illustrate the methodology and capabilities of the computer program and to assess the magnitudes of the chemical and vibrational nonequilibrium losses and the effect of the wall boundary layer on a generic hypersonic scramjet nozzle. Conclusions deduced from these calculations are in Sec. IV.

II. Basic Equations and Numerical Procedure

The computer program described in Refs. 2 and 3 was the starting point for the current analysis. (See also Ref. 4.) It employs the method of characteristics for rotational, nonhomentropic gas flows assuming frozen chemistry and neglecting diffusion. The extension of the basic equations in Refs. 2 and 3 to include turbulent mixing and finite-rate chemistry is discussed in Refs. 5 and 6. However, the direct nozzle design capability offered by the method of characteristics is not retained in the latter references. Of particular interest here are the modifications required to include finite-rate chemistry in the equations in Ref. 2. In this case, the two-dimensional, inviscid, planar or axisymmetric conservation equations are as follows:

Continuity:

$$\frac{\partial}{\partial x}(\rho u r^J) + \frac{\partial}{\partial r}(\rho v r^J) = 0 \tag{1}$$

Axial momentum:

$$\rho u \frac{\partial u}{\partial x} + \rho v \frac{\partial u}{\partial r} + \frac{\partial P}{\partial x} = 0 \tag{2}$$

Normal momentum:

$$\rho u \frac{\partial v}{\partial x} + \rho v \frac{\partial v}{\partial r} + \frac{\partial P}{\partial r} = 0 \tag{3}$$

Energy:

$$\rho u \frac{\partial H}{\partial x} + \rho v \frac{\partial H}{\partial r} = 0 \tag{4}$$

Species continuity:

$$\rho u \frac{\partial \alpha_i}{\partial x} + \rho v \frac{\partial \alpha_i}{\partial r} = \dot{\omega}_i \tag{5}$$

where, for the flows of interest here, the total enthalpy H includes sensible enthalpy, kinetic energy, *and* chemical enthalpy. Equations (1-5) are supplemented by an equation of state:

$$P = \rho R_o T \sum_i \frac{\alpha_i}{W_i} \tag{6}$$

Along the inviscid characteristic directions λ given by

$$\frac{\mathrm{d}y}{\mathrm{d}x} = \tan(\theta \pm \mu) \tag{7}$$

the compatibility equation may be written (Ref. 6) as

$$\frac{\sin\mu\cos\mu}{\gamma P}\,\mathrm{d}P \pm \mathrm{d}\theta = -\frac{J\sin\theta\sin\mu}{r}\,\mathrm{d}\lambda^{\pm} + F_{\lambda^{\pm}}\,\mathrm{d}\lambda^{\pm} \tag{8}$$

where (Ref. 5)

$$F_{\lambda}^{\pm} = \left(\frac{\gamma-1}{\gamma}\right)\left(\frac{\sin\mu}{PQ\cos(\theta\pm\mu)}\right)\cdot\sum_i \dot{\omega}_i\left(h_i\frac{W_i}{W} - c_p T\right) \tag{9}$$

The mixture specific heat is given by

$$c_p = \sum_i \alpha_i c_{p_i} \tag{10}$$

where c_{p_i} includes all internal degrees of freedom of a species i, and where

$$\gamma = \frac{c_p}{c_p - R/c_{p\infty}} \tag{11}$$

The effective Mach angle is defined by

$$\mu = \sin^{-1}\frac{1}{M} \tag{12}$$

where M is the local Mach number.

Details of the numerical procedure are contained in Ref. 2. The modifications introduced to incorporate finite-rate chemistry are as follows: consider the typical characteristic mesh shown in Fig. 1. Properties are known along the line AB, and the properties at point C are to be determined.

Procedures for the determination of the coordinates of point C are well documented (see, for example, Ref. 7). The results are as follows:

$$x_C = \frac{y_B - y_A + M_1 x_A - M_2 x_B}{M_1 - M_2} \tag{13a}$$

$$y_C = y_A + M_1(x_C - x_A) \tag{13b}$$

where $M_1 = M_1(\theta_A, \theta_C, \mu_A, \mu_c)$ and $M_2 = (\theta_B, \theta_C, \mu_B, \mu_C)$. The compatibility equation (8) may be written

$$P_C = \Big(A_1 P_A + B_1 P_B + \theta_A - \theta_B - (A_2 + B_2)x_C$$
$$+ A_2 x_A + B_2 x_B\Big)/(A_1 + B_1) \tag{14}$$

where

$$A_1 = \alpha\left(\frac{\sin\mu\cos\mu}{\gamma P}\right)_A + \beta\left(\frac{\sin\mu\cos\mu}{\gamma P}\right)_C \tag{15a}$$

$$B_1 = \alpha\left(\frac{\sin\mu\cos\mu}{\gamma P}\right)_B + \beta\left(\frac{\sin\mu\cos\mu}{\gamma P}\right)_C \tag{15b}$$

$$A_2 = J\left[\alpha\left.\frac{\sin\theta\sin\mu}{y\cos(\theta+\mu)}\right|_A + \beta\left.\frac{\sin\theta\sin\mu}{y\cos(\theta+\mu)}\right|_C\right]$$
$$-\left[\alpha\left.\frac{FR_{TH}}{\cos(\theta+\mu)}\right|_A + \beta\left.\frac{FR_{TH}}{\cos(\theta+\mu)}\right|_C\right] \tag{16a}$$

$$B_2 = J\left[\alpha\left.\frac{\sin\theta\sin\mu}{y\cos(\theta-\mu)}\right|_B + \beta\left.\frac{\sin\theta\sin\mu}{y\cos(\theta-\mu)}\right|_C\right]$$
$$-\left[\alpha\left.\frac{FR_{TH}}{\cos(\theta-\mu)}\right|_B + \beta\left.\frac{FR_{TH}}{\cos(\theta-\mu)}\right|_C\right] \tag{16b}$$

where, initially, $\alpha = 1$, $\beta = 0$, which fixes values at A, B, and D. After provisional properties at C are determined, a second iteration is performed with $\alpha = \beta = 0.5$. In Eqs. (16a) and (16b),

$$F_j = \left[\left(\frac{\gamma-1}{\gamma}\right)\left(\frac{\sin\mu}{PQ}\right)\cdot\sum_i \dot{\omega}_i\left(\frac{h_i W_i}{W} - c_p T\right)\right]_j \tag{17}$$

where $j = A$, B, or C and R_{TH} is the throat height (planar flow) or radius (axisymmetric flow).

By standard methods,[7] the flow inclination at C, θ_c, and the spatial location of point D are determined.

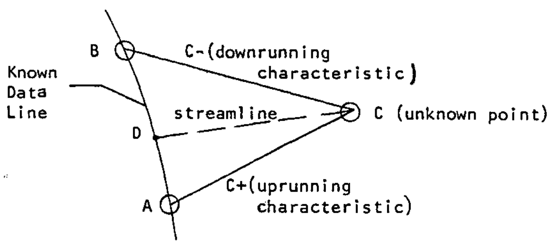

Fig. 1 Typical characteristic network.

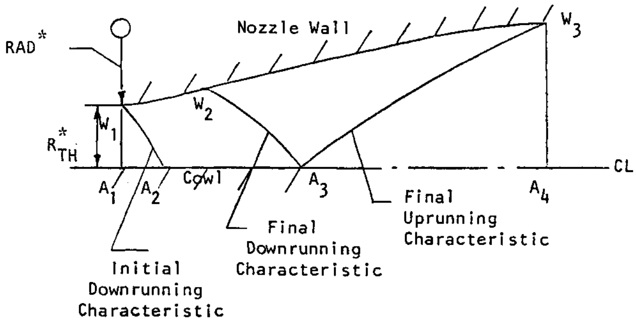

Fig. 2 Principal characteristics.

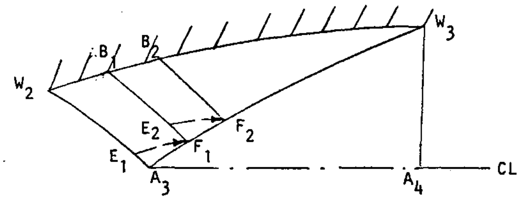

Fig. 3 Determination of the final uprunning characteristics.

The properties at D are obtained by linear interpolation between A and B. The velocity at C is then

$$q_C = q_D - \frac{2(P_C - P_D)}{[\alpha(\rho q)_D + \beta(\rho q)_C]} \tag{18}$$

and the temperature at C is

$$T_C = T_D + \frac{(\gamma_\infty - 1)M_\infty^2(P_C - P_D)}{\alpha(\rho c_p)_D + \beta(\rho c_p)_C} - \frac{\sum_i \left[(\alpha h_{i,D} + \beta h_{i,C})(\alpha_{i,C} - \alpha_{i,D})\right]}{\alpha c_{p,D} + \beta c_{p,C}} \tag{19}$$

The species concentrations at C are determined by utilization of the CREK code described by Pratt[8] along the streamline from D to C. The CREK code permits the introduction of either finite-rate chemistry or chemical equilibrium. The chemical kinetic mechanism employed in the calculations described herein, along with the associated rate coefficients, is in the Appendix. The mechanism was assembled by an examination of those in the literature for the H-O-N system extracting those likely to be important at the conditions under examination here. The reaction rate coefficients are primarily those of Baulch et al.,[9] supplemented as required by those in Ref. 10. It should be noted that CREK employs constant static pressure and static enthalpy in going from the initial to the final state; that is, in going from D to C herein. This pressure will be slightly different from that determined using Eq. (14), and the CREK-determined temperature at C will (slightly) differ as well from that obtained using Eq. (19). The predictor-corrector procedure employed in the present computer program is to use CREK to determine (to a good approximation) the composition at C using initial conditions at D, and then to use Eqs. (14) and (19) to determine P_C and T_C using the CREK-calculated composition at C. The computer program then performs a second iteration using the average pressure and enthalpy along the streamline based on the provisional solution at C.

Descriptions of the procedures used to calculate points along the nozzle axis and the nozzle wall are in Ref. 2. Also in Ref. 2 is a description of the procedure employed to design a perfectly expanded nozzle (i.e., exit flow parallel to the nozzle axis and at a uniform static pressure). The procedure described therein is applicable to frozen flows. A modification of this procedure was required for reacting flows as described in the following.

Referring to Fig. 2, the initial profile is specified along line W_1A_1 and is initially expanded by means of the circular arc W_1W_2 of radius RAD*. Downrunning characteristics emanating from the circular arc are generated until the characteristic W_2A_3 is obtained, which yields the design pressure or Mach number on the axis. In a frozen flow, the properties along the uprunning characteristic A_3W_3 may now be generated in their entirety by expanding the flow along the streamlines from W_2A_3 to the design pressure, with the mesh points along W_3A_3 determined by integration of the continuity equation. In a reacting flow, on the other hand, the uprunning characteristic W_3A_3 cannot be generated at this point in the computation since the composition has been changing along the streamlines from W_2A_3 to W_3A_3. The revised procedure is depicted in Fig. 3. The properties at F_1 (along W_3A_3) are determined in the manner indicated earlier, with the additional (modest) assumption that the composition at F_1 is the same as that at E_1, which is the first point above A_3 along W_2A_3. The uprunning characteristic F_1B_1 is completed, terminating at the nozzle wall (B_1). The composition at E_2, which is along F_1B_1, has been determined as part of the calculation generating F_1B_1. Mesh point F_2, also along W_3A_3, is now determined with the composition at F_2 taken to be the same as that at E_2. The uprunning characteristic F_2B_2 is now calculated. This procedure is repeated until the characteristic W_3A_3 has been completely generated. (The frozen composition assumption between the two characteristic mesh points described here is generally quite accurate provided a sufficiently small mesh spacing is selected. Numerical experimentation was carried out to aid in the determination of an appropriate mesh size.) The flow streamlines downstream of W_3A_3 are parallel to the axis (A_1-A_2-A_3-A_4), which permits the determination of the flow properties at the nozzle exit W_3A_4. Details of these calculations are in Ref. 2.

Vibrational nonequilibrium requires a reduction in the mixture internal energy (hence, mixture enthalpy) at C amounting to $\sum_i (u_{v,EQ} - u_v)_i^c \alpha_i^c$, in which the species vibrational energies at C, u_{vi}^c, are determined from

$$\frac{u_{v_i}^C - u_{v_i}^D i}{\Delta t} = \frac{1}{t_i}\left[u_{v,EQ} - u_v\right]_i^D \tag{20}$$

and the equilbrium vibrational energy terms (that is, if the vibrational temperature equaled the translational temperature) are obtained from the model for a simple harmonic oscillator:

$$u_{v,EQ,i} = \frac{R_i \Theta_i}{e^{\theta_i/T} - 1} \tag{21}$$

Diatomic- and triatomic-specie specific heats were corrected to account for vibrational nonequilibrium in accordance with

$$c_{p_i} = c_{p_i}(\text{curve fit value}) - \left[c_{p_{V,EQ}} - c_{p_v}\right]_i \tag{22}$$

where

$$c_{p_{v,EQ,i}} = R_i \left[\frac{\Theta_i/2T}{\sinh(\Theta_i/2T)}\right]^2 \tag{23}$$

$$c_{p_{v,i}} = R_i\left[\frac{\Theta_i/2T_{v,i}}{\sinh(\Theta_i/2T_{v,i})}\right]^2 \tag{24}$$

$$T_{v,i} = \frac{\Theta_i}{\ell n\left[1+\frac{R_i\Theta_i}{u_{v,i}}\right]} \tag{25}$$

and curve fit entropy values were corrected as follows:

$$s_i = s_i(\text{curve fit}) - \left[(u_{v,EQ} - u_v)_i/(T+T_{v,i})/2\right] \tag{26}$$

Quantities referred to as "curve fit" values including equilibrated vibrational modes (with anharmonic effects) were obtained from the fits in Ref. 11. Characteristic vibrational temperatues (Θ_i) and expressions used to obtain the vibrational relaxation times (t_i) are in the Appendix.

The direct coupling between the vibration and the chemistry, as discussed, for example, in Ref. 12, has been neglected here. In the case of strong shocks, where vibrational and translational temperatures can differ substantially downstream of the wave, this coupling has been shown to be important.[12] Large differences between vibrational and translational temperatures are not anticipated in the expanding flows of interest here; hence, this coupling is not believed to be a first-order effect.

Inviscid force and moment coefficients (per unit span) were calculated by trapezoidal rule integration of the surface pressures:

$$C_{F_x} = \int_0^{x_e} (P-P_\infty)_w \tan\theta_w \mathrm{d}x \tag{27}$$

$$C_{F_{y,\mathrm{wall}}} = \int_0^{x_e} (P-P_\infty)_w \, \mathrm{d}x \tag{28}$$

$$C_{F_{y,\mathrm{cowl}}} = \int_0^{x_c} (P-P_\infty)_c \, \mathrm{d}x \tag{29}$$

$$C_{M_x} = \int_0^{x_e} (P-P_\infty)_w (\tan\theta_w)(y-1) \, \mathrm{d}x \tag{30}$$

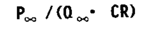

Fig. 4 Results of the one-dimensional cycle analysis.

Table 1 Start line properties

Specie	Mass Fraction
N_2	0.726244
O_2	0.002231
H_2O	0.220886
H_2	0.025865
O	0.002883
H	0.003443
OH	0.018515
HO_2	1.8587×10^{-6}

$P_o^* = 154.1$ KPa, $T_o^* = 3001$ K,
$V_o^* = 5759$ m/s, $R_{TH} = 2$ in. (0.0508 m)

$$C_{My,\mathrm{wall}} = \int_0^{x_e} (P-P_\infty)_w x \, \mathrm{d}x \tag{31}$$

$$C_{My,\mathrm{net}} = C_{My,\mathrm{wall}} - \int_0^{x_c} (P-P_\infty)_c x \, \mathrm{d}x \tag{32}$$

A compressible turbulent boundary-layer calculation, corresponding to the analysis of Ref. 13, is made at each calculated nozzle wall location to estimate boundary-layer displacement thickness, and skin friction coefficient. It should be noted that the previously described method-of-characteristics computations and this boundary-layer calculation are independent, except that the former supplies the flow conditions to the latter at the edge of the boundary layer. Hence, in an actual nozzle design, the inviscid nozzle wall calculated by the characteristics solution would be moved back by an amount equal to the calculated displacement thickness. In addition, the axial-force and moment coefficients (C_{Fx}, C_{Mx}) are corrected to account for the surface shear stress.

III. Results

In an effort to arrive at nozzle start line conditions that would be representative of an aerospace plane, yet would be independent of any specific current design, a one-dimensional cycle analysis code NUSCR (a derivative of the NASA LaRC, SCRAM, and COMBAN codes) was used to determine the flow properties through a generic hypersonic engine. The results of these calculations are summarized in Fig. 4, where a scaling parameter $P_o/(Q_\infty \cdot CR)$ is plotted as a function of flight Mach number and fuel-air equivalence ratio. (Note that P_o is freestream static pressure, Q_∞ is flight dynamic pressure, and CR is the engine inlet contraction ratio.) The point indicated in Fig. 4 corresponds to $[P_o/(Q_\infty \cdot CR)] = 4.0$, $M_\infty = 20.0$, $\phi = 2.0$. Nominal gas properties calculated by the cycle-analysis code at the nozzle entrance were then entered into a one-dimensional, streamtube chemistry code (SLCHEM) to generate a uniform start line in partial chemical equilibrium (i.e., NO was assumed not to be present based upon the observation that times required for NO formation in the combustor are considerably longer than hydrogen combustion times; see, for example Fig. 1 of Ref 10). The resulting start line is in Table 1.

Numerical experimentation led to the conclusion that a uniformly spaced 41-point start line gave results as numerically accurate and with as little mesh distortion as more densely spaced start lines (e.g., 81 points). Hence, 41-point start lines were employed throughout these studies.

Results for a two-dimensonal nozzle and a design exit pressure equal to the ambient pressure at an altitude of 144 kft (43.9 km) are shown in Figs. 5–14, with the sense of the moments taken as positive counterclockwise around point W_1 in

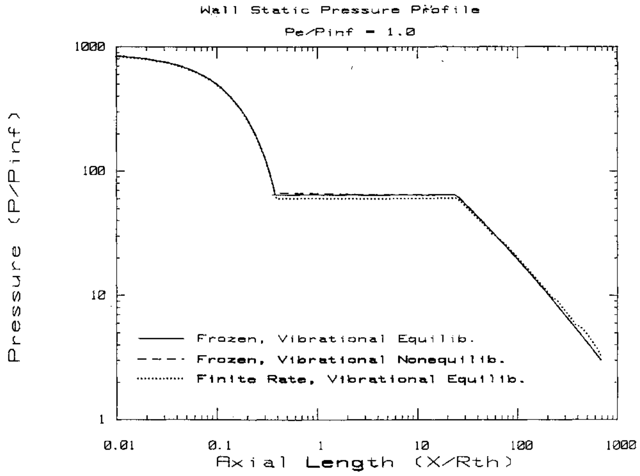

Fig. 5 Wall static pressure profile ($P_e/P_\infty = 1.0$).

Fig. 2. The wall and centerline static pressures are in Figs. 5 and 6, respectively. The initial wall pressure decrease out to a dimensionless axial distance of about 0.4 occurs along the initial circular arc section of the nozzle. In the transition region from the circular arc section (concave up) to the contoured section (concave down), the wall angle changes relatively little and the static pressure remains approximately constant out to a dimensionless axial distance of about 23.0 where the initial downrunning characteristics reflecting off the centerline meet the nozzle wall. The subsequent wall pressure decrease is the result of the continued expansion in the contoured section. The designed nozzles were truncated at a dimensionless x of 690, which, for the assumed 2-in. (0.0508 m) throat height, results in nozzle lengths of 115 ft (35.05 m). Along the nozzle centerline, the static pressure remains relatively constant until impacted by the downrunning characteristics from the circular arc section ($x/R_{TH} \approx 4$), after which the pressure drops until the region of uniform flow is reached at about $x/R_{TH} \approx 250$. (It should be noted that, since reactions continue in this "uniform" flow region, properties are, in fact, somewhat nonuniform here.)

The fact that the effects of vibrational relaxation are virtually negligible is of particular interest. Only in the nearly constant static temperature and pressure region ($0.4 \leq x/R_{TH} \leq 23.0$) can the vibrational equilibrium and nonequilibrium results be distinguished. On the other hand, the slightly higher wall static pressure values for the finite-rate case above $x/R_{TH} \approx 60.0$, which are a result of the recombination of dissociated species with an attendant energy recovery, have a relatively large impact on several of the force and moment coefficients. The axial force coefficient C_{Fx} in Fig. 7 illustrates once again the negligible effect of vibrational relaxation. As may be seen, however, the integrated effect of the higher wall static pressures in the finite-rate case results in appreciably higher values of C_{Fx}.

Viscous losses due to the wall boundary layer can also be seen to be appreciable. The boundary-layer calculation assumes that the physical nozzle wall has been recessed by an amount equal to the displacement thickness; hence, the decrement in C_{Fx} is solely a result of the integrated effect of the viscous wall shear stress (i.e., skin friction). These effects are magnified when determining the axial moment coefficient C_{Mx} in Fig. 8. Once again, however, vibrational nonequilibrium effects are negligible. Of interest in Fig. 7 is the fact that beyond a dimensionless axial distance of perhaps 300 to 400 there is little further increase in C_{Fx}, which may justify truncating this type of nozzle well before obtaining a substantial

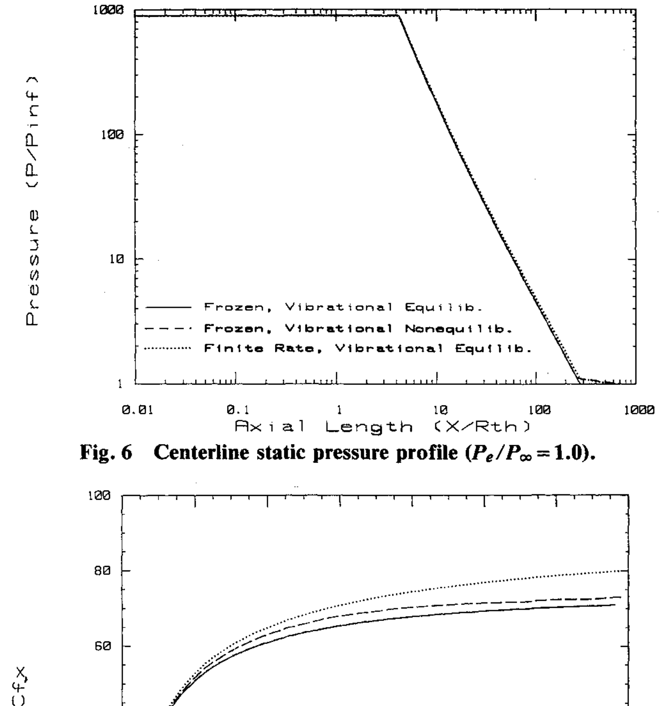

Fig. 6 Centerline static pressure profile ($P_e/P_\infty = 1.0$).

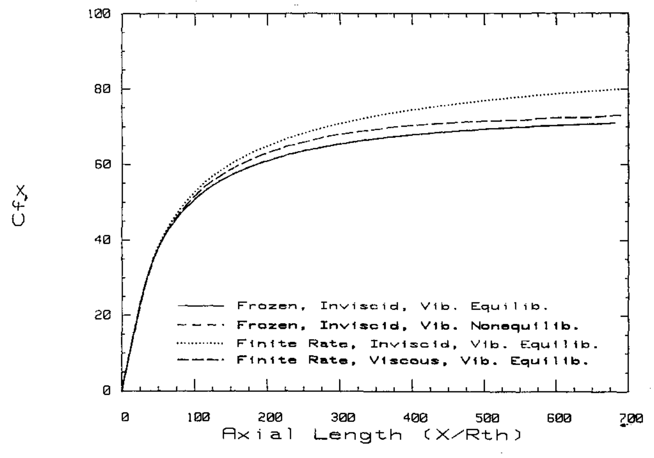

Fig. 7 Axial force coefficient profile ($P_e/P_\infty = 1.0$).

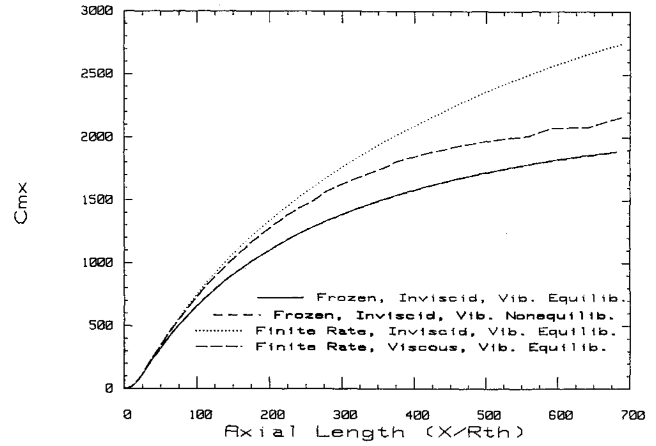

Fig. 8 Axial moment coefficient profile ($P_e/P_\infty = 1.0$).

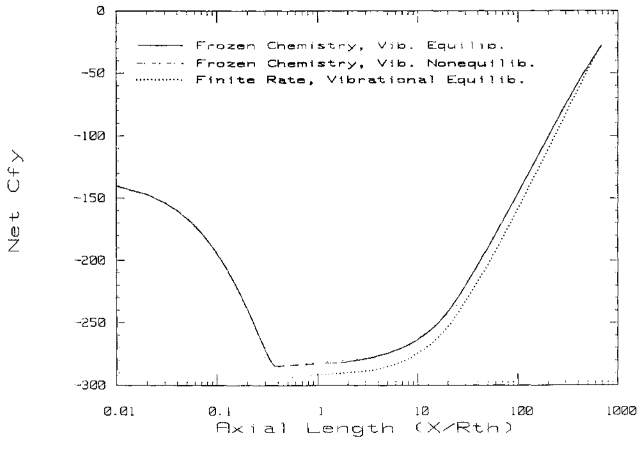

Fig. 9 Net normal force coefficient profile ($P_e/P_\infty = 1.0$).

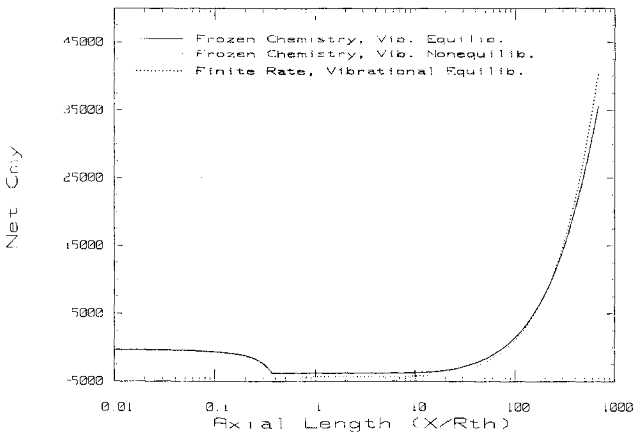

Fig. 10 Net normal moment coefficient profile ($P_e/P_\infty = 1.0$).

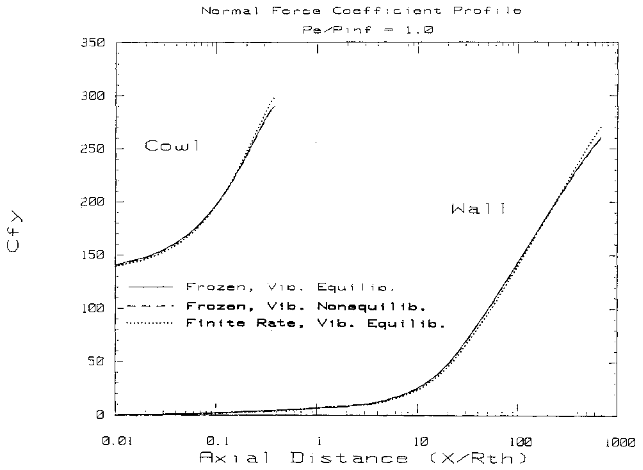

Fig. 11 Normal force coefficient profile ($P_e/P_\infty = 1.0$).

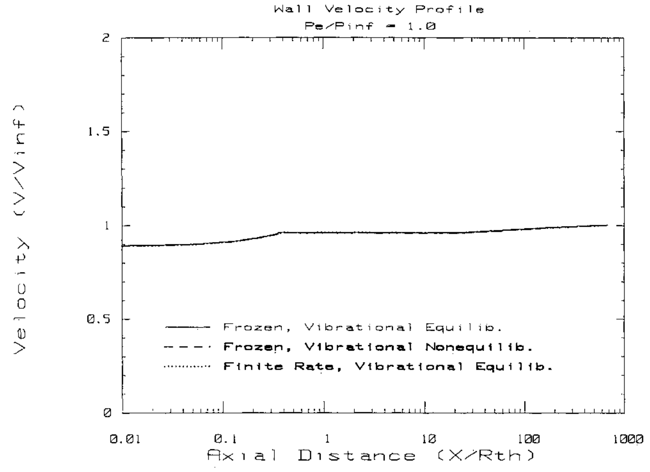

Fig. 12 Wall velocity profile ($P_e/P_\infty = 1.0$).

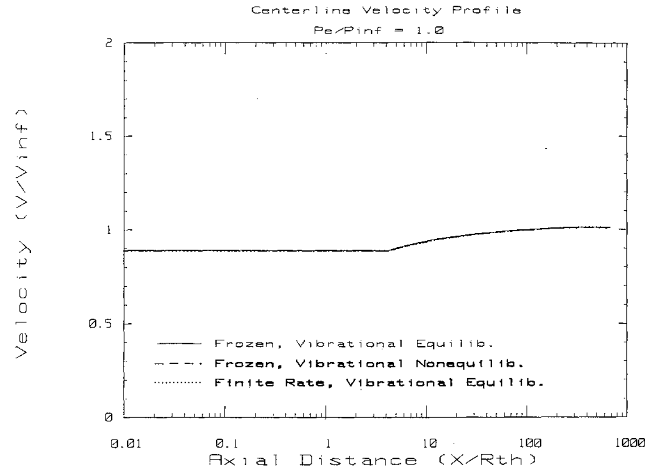

Fig. 13 Centerline velocity profile ($P_e/P_\infty = 1.0$).

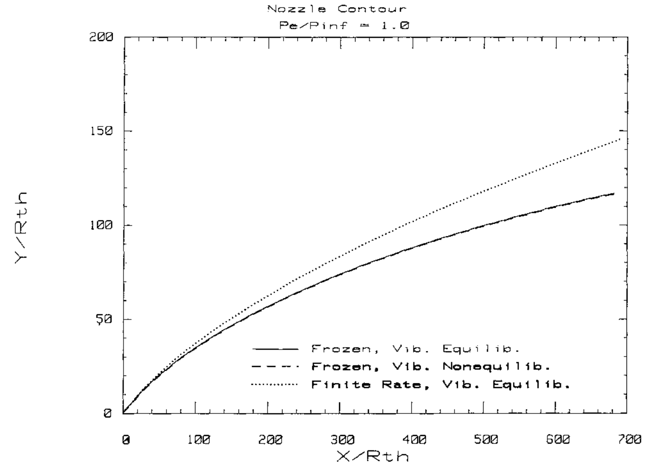

Fig. 14 Nozzle contour ($P_e/P_\infty = 1.0$).

region of uniform flow. (It may be anticipated that in some cases the cumulative skin friction drag will exceed the integrated pressure thrust beyond an optimum nozzle length.)

The results shown in Figs. 5–8 incorporate the conclusion in Ref. 9 that the probability of vibrational de-excitation under some nozzle flow conditions can be considerably greater than that encountered under normal shock conditions. Hence, the vibrational relaxation times of Ref. 14 have been divided by 15, as recommended in Ref. 15. To ensure that the conclusion that the vibrational mode is in equilibrium at the conditions examined here is independent of the findings of Ref. 15, an additional calculation was made using the vibrational relaxation times directly from Ref. 14 (i.e., without the division by 15). No significant differences result, leading to the conclusion that vibrational equilibrium is indeed predicted by these calculations.

The net normal force and moment coefficient profiles are shown in Figs. 9 and 10. A cowl is assumed to be present along the "centerline" from the throat to the point where the uniform flow region commences at the centerline. (That is, to the location where the downrunning characteristic yielding the design condition meets the centerline; see Fig. 2.) The pressure on the cowl leads to large negative normal force and moment coefficients up to a dimensionless axial length of about 0.3 to 0.4, which is about where the initial circular arc terminates. This is illustrated in Fig. 11. After the region of relatively constant pressure and temperature, C_{Fy} and C_{My} rapidly increase; in the case of the latter, reaching very large positive values at the nozzle truncation location. Note also the relatively appreciable effect of species recombination on C_{Fy} and C_{My}, and the negligible effect of vibrational nonequilibrium.

Wall and centerline velocity profiles, shown in Figs. 12 and 13, illustrate the insensitivity of velocity to chemical effects. However, substantially different nozzle contours result as a consequence of the chemistry, as shown in Fig. 14.

The aforementioned results make clear that vehicle trim requirements will be greatly affected by finite-rate nozzle recombination and boundary-layer effects, and that these effects can be accurately ascertained only by calculations that deal with the two dimensionality of the flowfield.

Effect of Changing the Design Exit Pressure Ratio

Since the nozzle design employed here calls for truncating the nozzle at a specified axial distance, other parameters can be varied to produce nozzles having characteristics deemed to be important by the engine designer. For example, the effects on the nozzle design and performance of changes in the specified value of exit pressure are shown in Figs. 16–21. As shown in Fig. 15, increasing the design exit pressure will decrease the exit height (i.e., exit cross-sectional area) at the truncation plane and result in a larger uniform flow region as well. The exit height effect is shown in Fig. 16 and is seen to be appreciable. Increasing the design exit pressure leads to the behavior shown in Fig. 17 of the boundary-layer displacement thickness, and to an increased axial force coefficient, as shown in Fig. 18. In the case of the viscous corrected C_{Fx}, an increase of nearly 11% results from increasing the design exit pressure from one-half of P_∞ to twice P_∞ for the finite-rate calculations. On the other hand, the geometric changes in the nozzle contour lead to a reduction in C_{Mx} as the design exit pressure increases (see Fig. 19).

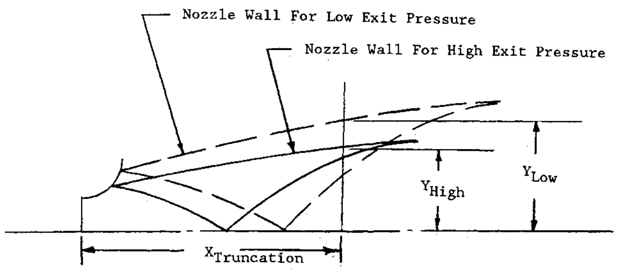

Fig. 15 Schematic illustrating the effects of changing the specified design exit pressure.

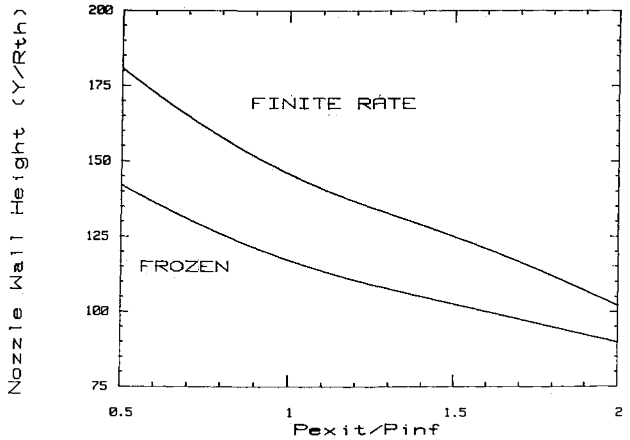

Fig. 16 The effect of design exit pressure on nozzle length.

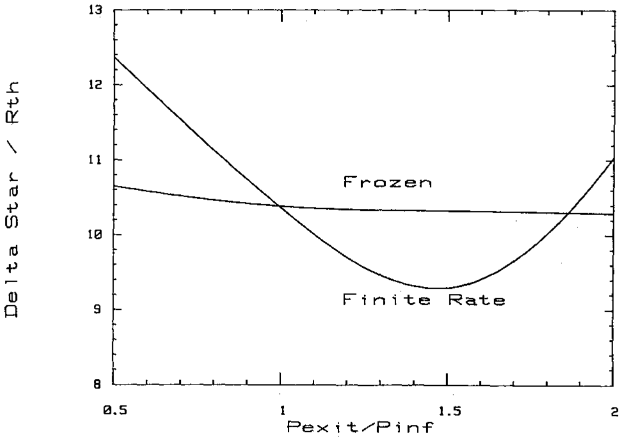

Fig. 17 The effect of design exit pressure on boundary-layer displacement thickness.

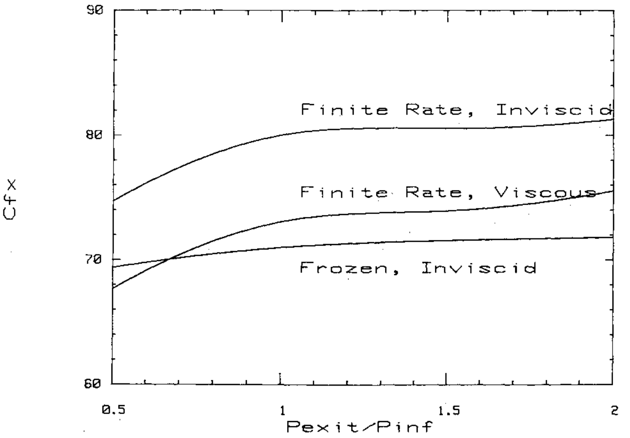

Fig. 18 The effect of design exit pressure on axial force coefficient.

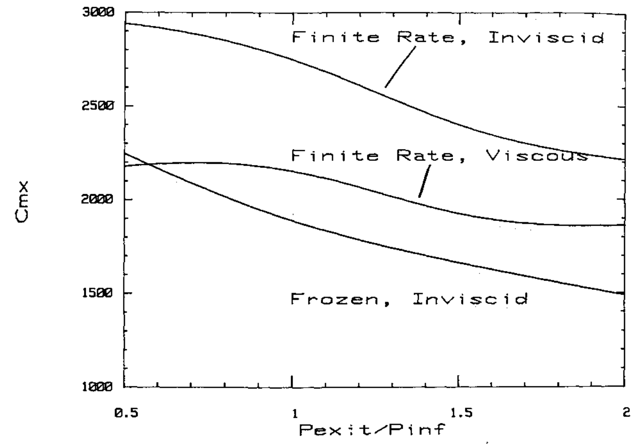

Fig. 19 The effect of design exit pressure on axial moment coefficient.

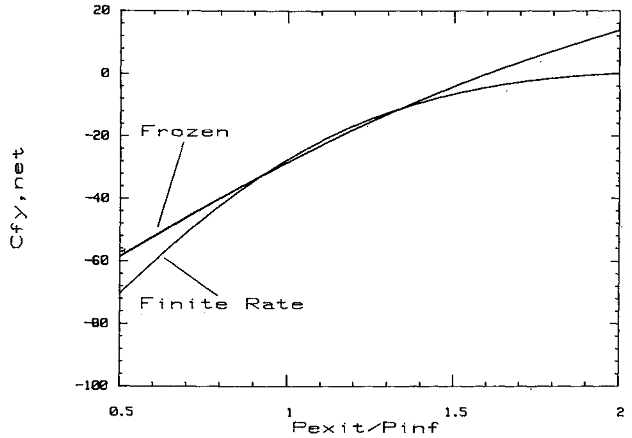

Fig. 20 The effect of design exit pressure on normal force coefficient.

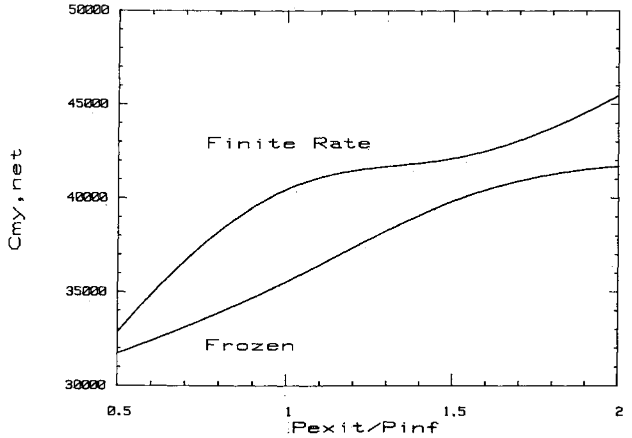

Fig. 21 The effect of design exit pressure on normal moment coefficient.

The calculations indicate that increasing P_e, which tends to shorten the cowl length, results in an increase in the net normal force coefficient C_{Fy} and net normal moment coefficient C_{My} (Figs. 20 and 21). Indeed, the finite-rate calculations indicate that for a P_e/P_∞ of 2.0, the net normal force is nearly zero.

These results make it clear that a wide variety of nozzle geometries and performance characteristics can be obtained by proper selection of the controllable design parameters. In addition to P_e, a maximum permissible wall angle can be specified, although none were in these calculations.

IV. Concluding Remarks

A frozen-chemistry, method-of-characteristics computer program for designing and analyzing propulsion engine nozzles has been expanded to incorporate finite-rate chemistry and vibrational relaxation. In addition, appended to the code is a compressible, turbulent boundary-layer calculation modeled after the analysis in Ref. 13, which estimates such parameters as boundary-layer displacement thickness, skin friction coefficient, and surface heat-transfer coefficient along the nozzle wall. The code was used herein to design a generic, two-dimensional nozzle for a NASP-type vehicle based upon an arbitrarily selected flight condition. An assessment of the various effects examined leads to the following conclusions.

1) Nozzle design and performance estimates must be made on the basis of a finite-rate chemistry calculation since a frozen-chemistry assumption will result in significantly lower performance estimates for the nozzles.

2) Viscous effects (wall boundary layer) are also significant and must be accounted for in designing nozzles and assessing their performance.

3) Vehicle trim requirements must be determined from calculations that include both finite-rate chemistry and viscous effects.

4) Vibrational relaxation times appear to be quite short at these conditions; hence, the flow appeared to be in vibrational equilibrium throughout its passage through the nozzle.

5) Beyond a certain axial location, which is considerably upstream of the nozzle exit station (i.e., where a "uniform," parallel flow exists), little additional axial thrust is obtained. The added length past this station does, however, significantly affect the normal force coefficient and its associated pitching moment. The latter will significantly affect vehicle trim requirements. These considerations, as well as those of vehicle length, weight, etc., may militate in favor of truncating the nozzle well short of its nominal exit station.

Appendix

Table A1 Chemical kinetic mechanism and forward reaction rate coefficients

Forward reaction		Reverse reaction			Forward rate coefficient		
					A′	N	E
H_2	M	H	H	M	11.342	0.0	48300.00
O_2	M	O	O	M	15.860	−1.0	59340.00
H_2O	M	OH	H	M	13.342	0.0	52900.00
OH	M	O	H	M	15.930	−1.0	50830.00
H	O_2	HO_2		M	9.362	0.0	−402.60
H_2O	O	OH	OH	—	10.833	0.0	9240.00
H_2O	H	OH	H_2	—	10.968	0.0	10250.00
O_2	H	OH	O	—	11.342	0.0	8450.00
H_2	O	OH	H	—	9.570	0.0	4480.00
H_2	O_2	OH	OH	—	10.000	0.0	21540.70
H_2	O_2	HO_2	H	—	10.740	0.0	29100.00
H	HO_2	OH	OH	—	11.380	0.0	949.67
H_2O	O	H	HO_2	—	8.763	0.5	28686.50
O	HO_2	OH	O_2	—	10.699	0.0	503.27
OH	HO_2	H_2O	O_2	—	10.477	0.0	0.00
H_2	HO_2	H_2O	OH	—	10.301	0.0	12581.80

Note: The rate coefficient is given by $k_f = AT^N \exp(-E/RT)$, where $A = 10^{A'}$ (m^3/kgmole/s), $R = 1.987$ cal/gmole/K and E is in cal/gmole.

Table A2 Vibrational relaxation parameters

Species	Characteristic vibrational temperature, K
H_2	6140
H_2O	5036
N_2	3340
OH	5036
O_2	2260
HO_2	5036

Vibrational relaxation times (from Ref. 15)

$$t_{O_2-O_2}p = \frac{1.97\times 10^{-16}T^{5/6}}{(1-e^{-2228/T})}\cdot \exp(218.3/T^{1/3})\text{atm-s} \tag{A1}$$

$$t_{O_2-M} = 5t_{O_2-O_2} \tag{A2}$$

$$t_{N_2}p = \frac{6.4\times 10^{-13}T^{1/2}}{(1-e^{-3336.6/T})}\cdot \exp(192.0/T^{1/3})\text{atm-s} \tag{A3}$$

From Eqs. (A1) and (A2):

$$Z = y_{O_2}t^{-1}_{O_2-O_2} + (1-y_{O_2})t^{-1}_{O_2-M} \tag{A4}$$

$$t_{O_2} = Z^{-1} \tag{A5}$$

For other polyatomic species:

$$t_i = 0.5(t_{O_2} + t_{N_2}) \tag{A6}$$

Acknowledgment

This work was sponsored by the National Aerospace Plane Joint Program Office, Wright-Patterson AFB, Ohio 45433-6503.

References

[1] Vincenti, W. G. and Kruger, C. H., Jr., *Introduction to Physical Gas Dynamics,* R. E. Krieger Publishing Co., Malabar, FL, 1965, pp. 293-300.

[2] Dash, S., "The Determination of Nozzle Contours for Rotational, Non-Homentropic Gas Mixtures," Advanced Technology Laboratories, Inc., Rept. ATL-TR148, March 1970.

[3] Kalben, P., "A Fortran Program for the Determination of Nozzle Contours for Rotational, Non-Homentropic Gas Mixtures," Advanced Technology Laboratories, Inc., Rept. ATL-TM148a, April 1970.

[4] Zucrow, M. J. and Hoffman, J. D., *Gas Dynamics,* Vols. 1 and 2, Wiley, New York, 1976-1977.

[5] Dash, S. M., Sinha, N., and York, B. J., "Implicit/Explicit Analysis of Interactive Phenomena in Supersonic, Chemically Reacting, Mixing and Boundary Layer Problems," AIAA Paper 85-1717, July 1985.

[6] Sinha, N. and Dash, S. M., "Parabolized Navier-Stokes Analysis of Ducted Turbulent Mixing Problems with Finite-Rate Chemistry," AIAA Paper 86-0004, Jan. 1986.

[7] Emanuel, G., *Gas Dynamics: Theory and Applications,* AIAA, New York, 1986, pp. 283-303.

[8] Pratt, D. T., "Calculation of Chemically Reacting Flows with Complex Chemistry," *Studies in Convection,* Vol. II, edited by B. F. Launder, Academic Press, New York, 1976.

[9] Baulch, D. L., Drysdale, D. D., Horne, D. G., and Lloyd, A. C., *Evaluated Kinetic Data for High Temperature Reactions,* Vol. 1, CRC Press, Cleveland, OH, 1972.

[10] Rogers, R. C. and Schexnayder, C. J., Jr., "Chemical Kinetic Analysis of Hydrogen-Air Ignition and Reaction Times," NASA TP-1856, July 1981.

[11] McBride, B. J., Heimel, S., Ehlers, J. G., and Gordon, S., "Thermodynamic Properties to 6000°K for 210 Substances Involving the First 18 Elements," NASA SP-3001, 1963.

[12] Treanor, C. E. and Marrone, P. V., "Effect of Dissociation on the Rate of Vibrational Relaxation," *Physics of Fluids,* Vol. 5, Sept. 1962, pp. 1022-1026.

[13] Sasman, P. K. and Cresci, R. J., "Compressible Turbulent Boundary Layer with Pressure Gradient and Heat Transfer," *AIAA Journal,* Jan. 1966, pp. 19-25.

[14] Wood, A. D., Springfield, J. F., and Pallone, A. J., "Determination of the Effects of Chemical and Vibrational Relaxation on an Inviscid Hypersonic Flow Field," AIAA Paper 63-441, Aug. 1963.

[15] Hurle, I. R., Russo, A. L., and Hall, J. G., "Spectroscopic Studies of Vibrational Nonequilibrium in Supersonic Nozzle Flows," *Journal of Chemical Physics,* Vol. 40, No. 8, April 1964, pp. 2076-2089.